Journal of Computational Physics 229 (2010) 6300–6317

Contents lists available at ScienceDirect

Journal of Computational Physics

journal homepage: www.elsevier.com/locate/jcp

A conservative immersed interface method for Large-Eddy Simulation of incompressible flows

M. Meyer *, A. Devesa, S. Hickel, X.Y. Hu, N.A. Adams

Technische Universität München, Institute of Aerodynamics, 85747 Garching, Germany

ARTICLE INFO

Article history:
Received 31 August 2009
Received in revised form 25 February 2010
Accepted 24 April 2010
Available online 4 May 2010

Keywords:
Immersed interface method
Immersed boundary method
Large-Eddy Simulation

ABSTRACT

We propose a conservative, second-order accurate immersed interface method for representing incompressible fluid flows over complex three dimensional solid obstacles on a staggered Cartesian grid. The method is based on a finite-volume discretization of the incompressible Navier–Stokes equations which is modified locally in cells that are cut by the interface in such a way that accuracy and conservativity are maintained. A level-set technique is used for description and tracking of the interface geometry, so that an extension of the method to moving boundaries and flexible walls is straightforward. Numerical stability is ensured for small cells by a conservative mixing procedure. Discrete conservation and sharp representation of the fluid–solid interface render the method particularly suitable for Large-Eddy Simulations of high-Reynolds number flows. Accuracy, second-order grid convergence and robustness of the method is demonstrated for several test cases: inclined channel flow at $Re = 20$, flow over a square cylinder at $Re = 100$, flow over a circular cylinder at $Re = 40$, $Re = 100$ and $Re = 3900$, as well as turbulent channel flow with periodic constrictions at $Re = 10{,}595$.

© 2010 Elsevier Inc. All rights reserved.

1. Introduction

The generation of suitable body-fitted grids for Large-Eddy Simulation (LES) of complex flows can be time-consuming and difficult. Contradictory requirements, such as adequate local resolution and minimum number of grid points, can deteriorate the grid quality and therefore adversely affect accuracy and numerical convergence properties. Unstructured grids without rather severe constraints on cell size and aspect ratio, however, are known to be not well suited for time-resolving turbulent-flow computations, in particular for LES. An alternative approach is to use Cartesian grids, which also facilitates automatic grid generation and local grid refinement. Cartesian grids imply fewer computational operations per grid point than body-fitted or unstructured grids. On the other hand, bounding surfaces of the flow or immersed obstacles need to be accounted for by mapping the boundaries onto the grid. The formulation of accurate interface conditions at boundaries that are not aligned with the grid is a major challenge. Approaches, which have been proposed in literature, can be classified into continuous and discrete forcing approaches [38].

In the continuous forcing approach [44], a distributed forcing function is inserted into the momentum equations to mimic the interaction at the interface. The forcing function contains model parameters that have to be adapted to the flow configuration. Various extensions and adaptations have been proposed [18,30,32,45,48]. Disadvantages of this approach are that sharp interfaces are smeared over an area corresponding to the local mesh width [46] and the lack of discrete conservation. An application to solid boundaries can lead to stability and accuracy issues due to the stiffness of the forcing function [32,51].

* Corresponding author. Tel.: +49 89 289 16151; fax: +49 89 289 16139.
E-mail address: michael.meyer@aer.mw.tum.de (M. Meyer).

0021-9991/$ - see front matter © 2010 Elsevier Inc. All rights reserved.
doi:10.1016/j.jcp.2010.04.040

Mohd-Yusof [39] and Verzicco et al. [61] developed a predictor–corrector formulation for enforcing a wall boundary condition with a discrete forcing function in the momentum equations. Whereas accurate representation of the boundary has been demonstrated, the approach also lacks discrete conservativity. Ghost-cell approaches [55] and reconstruction methods [28,30,34,43] both use interpolation to impose the boundary conditions at the interface. While the former extrapolates velocity and pressure field to ghost cells based on nearby fluid points to enforce the boundary condition, the latter reconstructs the velocity field near the immersed boundary. Both methods are attractive because of their simplicity. However, in general these methods do not conserve discrete momentum and mass in the vicinity of the interface [28,30].

Another discrete forcing approach is the cut-cell method introduced first for inviscid flows by Clarke [5], later extended to viscous flows [57–59,62]. Cells cut by the immersed interface are truncated so that they conform to the shape of the boundary surface. The cut-cell method is based on a finite-volume discretization and generally maintains discrete conservation. A sharp representation of the immersed interface can be achieved. A common problem of cut-cell methods is the creation of very small fluid cells that lead to numerical instability if left untreated [29]. However, this approach seems the most appropriate for dealing with turbulent flows when an accurate representation of the flow in the vicinity of the immersed interface is required. Colella et al. [6,27] applied the cut-cell method to free surface flows in three dimensions on a collocated grid. Ye et al. [62] proposed a finite-volume collocated-grid formulation for incompressible fluid flows, where the fluid part of cut cells, whose center is located within the solid, is merged with adjacent fluid cells. To ensure second-order accuracy, the flux calculation requires an interpolation of the cell variables and their gradients at the cell faces near the boundary. The method has been applied to simulate various two-dimensional flows with stationary and moving boundaries [36,37]. Chung [4] modified the cell merging approach of [62] for improving the shape resolution of the immersed interface. However, second-order grid convergence has not been achieved.

For the incompressible Navier–Stokes equations pressure–velocity coupling is an essential concern. Unlike with collocated grids, approaches based on staggered grids allow for a consistent finite-volume discretization of the divergence-free constraint and have favorable stability properties [15]. Only few cut-cell methods for staggered grids have been reported in literature: Tau [52] and Tucker and Pan [56] addressed two-dimensional problems with first-order accuracy at the boundaries. Kirkpatrick et al. [29] presented a three-dimensional method on staggered grids, where advective fluxes and diffusive fluxes of the cut cells are modified. The small-cell problem is addressed by linking small cells and adjacent fully fluid cells to form a master–slave pair. Boundary conditions for the pressure at the immersed boundary are not imposed directly but with the projection method of Bell et al. [1], requiring several inner and outer iteration loops. Dröge and Verstappen [10,11] propose a method motivated by preserving the symmetry of the convective and diffusive operators. The authors emphasize that boundary conditions at the immersed interfaces cannot be defined without adversely influencing either the symmetry of the operators or global accuracy. Both the method of Kirckpatrick et al. and the method of Dröge and Verstappen achieve second-order spatial accuracy and show good results for flows with solid boundaries. However, for moving boundaries and fluid–structure interaction problems, not only conservativity but also a more simple representation of the geometry, e.g. based on a level-set field, is desirable.

The purpose of this paper is to develop an efficient, conservative, second-order accurate Cartesian cut-cell method for the incompressible Navier–Stokes equations on three-dimensional non-uniform staggered grids which is suitable for the extension to moving boundaries and fluid–structure interaction. The approach is applicable to any finite-volume discretization on a staggered grid. Finite-volume fluxes for cut cells and fluid cells are treated in the same manner, only cut cells are subjected to subsequent modification. The pressure boundary condition is imposed directly without computational overhead in the pressure-Poisson solver. To ensure numerical stability for small cells, we essentially follow the conservative mixing procedure proposed by Hu et al. [26]. A level-set field describes the interface geometry, so that an extension to moving boundaries and more complex configurations is straightforward. Accordingly, we call this method Conservative Immersed Interface Method (CIIM). We also provide evidence that this method is suitable for Large-Eddy Simulation (LES) of wall-bounded flows.

In Section 2.1 we summarize the underlying spatial and temporal discretization of the governing equations. The Immersed Interface Method is derived in Section 2.2. An overview of the implementation is given in Section 2.3. Numerical examples including validation results are presented and discussed in Section 3. Concluding remarks are given in Section 4.

2. Method

Our method consists of two parts: an underlying finite-volume discretization applied to all cells of the entire computational domain and a special procedure applied only to the cut cells. For simplicity, the method is developed in the following for non-moving boundaries. An extension to moving boundary cases is straightforward.

2.1. Underlying finite-volume discretization

We consider a generic conservation equation in differential form on the domain Ω

$$\partial_t \mathbf{\Phi} + \nabla \cdot \mathbf{F} = 0, \tag{1}$$

where $\mathbf{\Phi}$ represents a conserved quantity and $\mathbf{F}$ is a flux function. The Navier–Stokes equations for incompressible fluid flow are recovered when $\mathbf{\Phi}$ equals the velocity $\mathbf{u} = [u, v, w]$ and $\mathbf{F}$ is the nonlinear flux function

$$\mathbf{F} = \mathbf{uu} + \mathbf{I}p - \nu\nabla\mathbf{u}, \tag{2}$$

where ν represents the kinematic viscosity, p is the pressure and $\mathbf{I}$ is the unity tensor. Note that the non-dimensional constant density is $\rho = 1$. Mass conservation on Ω is ensured by

$$\nabla \cdot \mathbf{u} = 0. \tag{3}$$

A finite-volume discretization of Eq. (1) is obtained by

$$\frac{1}{V_{i,j,k}\Delta t}\int_{t_n}^{t_{n+1}} dt \int_{V_{i,j,k}\cap\Omega} dx\,dy\,dz\left(\frac{\partial \mathbf{u}}{\partial t} + \nabla\cdot\mathbf{F}\right) = 0, \tag{4}$$

where $V_{i,j,k}\cap\Omega$ is a computational cell (i,j,k) of a Cartesian grid. Time integration is performed from step t_n to t_{n+1} with time step size $\Delta t = t_{n+1} - t_n$. Volume-averaged quantities $\bar{\mathbf{u}}$ are defined as

$$\bar{\mathbf{u}}_{i,j,k} = \frac{1}{V_{i,j,k}}\int_{V_{i,j,k}\cap\Omega} \mathbf{u}_{i,j,k}\,dx\,dy\,dz. \tag{5}$$

Discretizing Eq. (4) in time by an Euler forward scheme, which corresponds to a substep of the Runge–Kutta scheme used later, results in

$$\frac{\bar{\mathbf{u}}^{n+1}_{i,j,k} - \bar{\mathbf{u}}^{n}_{i,j,k}}{\Delta t} = \frac{1}{V_{i,j,k}}\int_{V_{i,j,k}\cap\Omega} \nabla\cdot\mathbf{F}(\bar{\mathbf{u}}^n, \bar{p}^n)_{i,j,k}\,dx\,dy\,dz. \tag{6}$$

The divergence-free condition Eq. (3) is enforced by a fractional-step method with the intermediate velocity

$$\bar{\mathbf{u}}^{\star}_{i,j,k} = \bar{\mathbf{u}}^{n}_{i,j,k} + \frac{\Delta t}{V_{i,j,k}}\int_{V_{i,j,k}\cap\Omega} \nabla\cdot\mathbf{F}(\bar{\mathbf{u}}^n, \bar{p}^n)_{i,j,k}\,dx\,dy\,dz, \tag{7}$$

where $\mathbf{F}(\bar{\mathbf{u}}^n_{i,j,k}, \bar{p}^n)$ includes a predictor for the pressure gradient using the pressure at time step n. For pressure projection a Poisson equation

$$\nabla^2\bar{\phi}_{i,j,k} = -\nabla\cdot\bar{\mathbf{u}}^{\star}_{i,j,k}, \tag{8}$$

is solved, leading to a divergence-free velocity field

$$\bar{\mathbf{u}}^{n+1}_{i,j,k} = \bar{\mathbf{u}}^{n}_{i,j,k} - \nabla\bar{\phi}_{i,j,k}. \tag{9}$$

Finally the pressure is updated by

$$\bar{p}^{n+1}_{i,j,k} = \bar{p}^{n} + \frac{\bar{\phi}_{i,j,k}}{\Delta t}. \tag{10}$$

By the Gauss theorem, the right-hand-side of Eq. (7) becomes

$$\bar{\mathbf{u}}^{\star}_{i,j,k} = \bar{\mathbf{u}}^{n}_{i,j,k} + \frac{\Delta t}{V_{i,j,k}}\int_{\partial(V_{i,j,k}\cap\Omega)} \mathbf{F}(\bar{\mathbf{u}}^n, \bar{p}^n)_{i,j,k}\cdot\mathbf{n}_{\perp}\,dS, \tag{11}$$

where $\partial(V_{i,j,k}\cap\Omega)$ is the surface of $V_{i,j,k}\cap\Omega$, i.e. the six finite-volume cell faces intersecting with the Cartesian grid at $(x_i \pm \Delta x/2, y_i, z_i)$, $(x_i, y_i \pm \Delta y/2, z_i)$, and $(x_i, y_i, z_i \pm \Delta z/2)$. The normal vector on the cell faces is $\mathbf{n}_{\perp}$. From Eq. (11) we obtain finally

$$\begin{aligned}\bar{\mathbf{u}}^{\star}_{i,j,k} = \bar{\mathbf{u}}^{n}_{i,j,k} &+ \frac{\Delta t}{\Delta x}\left[\overline{\mathbf{F}}_{i+1/2,j,k} - \overline{\mathbf{F}}_{i-1/2,j,k}\right] \\ &+ \frac{\Delta t}{\Delta y}\left[\overline{\mathbf{F}}_{i,j+1/2,k} - \overline{\mathbf{F}}_{i,j-1/2,k}\right] \\ &+ \frac{\Delta t}{\Delta z}\left[\overline{\mathbf{F}}_{i,j,k+1/2} - \overline{\mathbf{F}}_{i,j,k-1/2}\right],\end{aligned} \tag{12}$$

where $\overline{\mathbf{F}}_{i\pm1/2,j,k}$, $\overline{\mathbf{F}}_{i,j\pm1/2,k}$, $\overline{\mathbf{F}}_{i,j,k\pm1/2}$ are the face-averaged fluxes at the cell faces. Eq. (12) corresponds to a standard finite-volume discretization on a three-dimensional Cartesian grid. In this paper, fluxes in Eq. (12) are computed with the Adaptive Local Deconvolution Method (ALDM), which for non-turbulent flows corresponds to a standard central second-order finite-volume scheme, whereas for turbulent flows it provides a subgrid-scale model implicitly [21–25]. For the following subsections it is important to keep in mind that the momentum equations are discretized on a staggered grid (see Fig. 1).

2.2. Conservative Immersed Interface Method (CIIM)

The flux balance in Eq. (12) must be modified appropriately for cells that are cut by an interface, see Fig. 2. For cut cells the wetted surface is defined by the unity of the fraction of the six cell faces wetted by the fluid and the subset of the interface

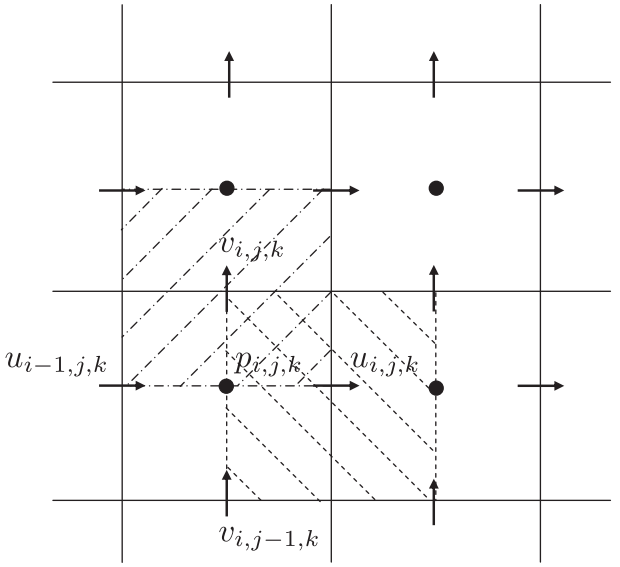

Fig. 1. U control volume (– –), v control volume (· – ·) and p control volume of a cell on a staggered grid in 2D; arrows indicate locations of velocity components, circles locations of pressure.

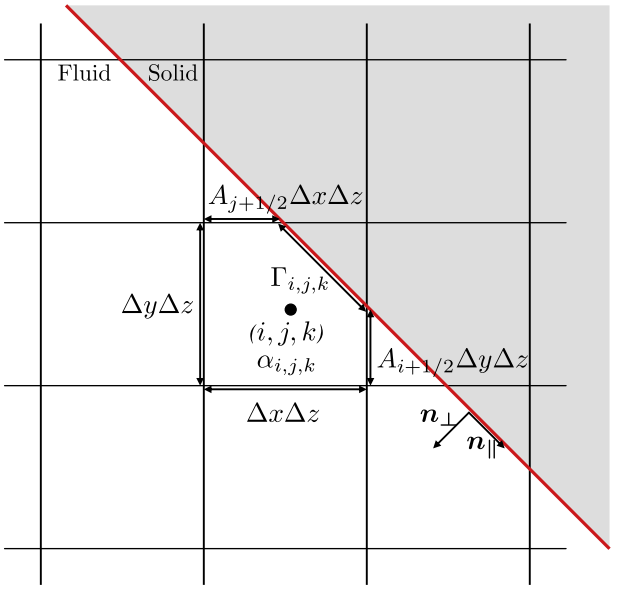

Fig. 2. Fluid volume fraction $\alpha_{i,j,k}$, intersection of $\partial(V_{i,j,k} \cap \Omega)$ and interface with cell $\Gamma_{i,j,k}$, for the cut cell (i, j, k).

contained in the cell $V_{i,j,k} \cap \Omega$. The latter is approximated by a planar element $\Gamma_{i,j,k}$. At the interface $\Gamma_{i,j,k}$ the no-slip conditions for the normal velocity $\bar{\mathbf{u}}_\perp = (\bar{\mathbf{u}} \cdot \mathbf{n}_\perp)\mathbf{n}_\perp = 0$ and the tangential velocity components $\bar{\mathbf{u}}_\parallel = \bar{\mathbf{u}} - \bar{\mathbf{u}}_\perp = 0$ and the Neumann condition for pressure $\nabla\bar{p} \cdot \mathbf{n}_\perp = 0$ must be satisfied.

2.2.1. Volume balance

For the cut cells the finite-volume formulation is maintained by taking into account face apertures, volume fraction and the interface segment $\Gamma_{i,j,k}$. The fluid volume fraction of a cut cell is denoted as $\alpha_{i,j,k}$ with $0 \leqslant \alpha_{i,j,k} \leqslant 1$. The wetted segment of the cell faces can be written as $A_{i\pm1/2,j,k}\Delta y\Delta z$, $A_{i,j\pm1/2,k}\Delta x\Delta z$, and $A_{i,j,k\pm1/2}\Delta x\Delta y$, where $0 \leqslant A_{l,m,n} \leqslant 1$ are the face apertures. Accordingly, the fluid volume of a cell is $V_{i,j,k} = \alpha_{i,j,k}\Delta x\Delta y\Delta z$. Eq. (12) can be rewritten as

$$\begin{aligned}\bar{\mathbf{u}}^{\star}_{i,j,k} = \bar{\mathbf{u}}^{n}_{i,j,k} &+ \frac{\Delta t}{\alpha_{i,j,k}\Delta x}\left[A_{i+1/2,j,k}\overline{\mathbf{F}}_{i+1/2,j,k} - A_{i-1/2,j,k}\overline{\mathbf{F}}_{i-1/2,j,k}\right] \\ &+ \frac{\Delta t}{\alpha_{i,j,k}\Delta y}\left[A_{i,j+1/2,k}\overline{\mathbf{F}}_{i,j+1/2,k} - A_{i,j-1/2,k}\overline{\mathbf{F}}_{i,j-1/2,k}\right] \\ &+ \frac{\Delta t}{\alpha_{i,j,k}\Delta z}\left[A_{i,j,k+1/2}\overline{\mathbf{F}}_{i,j,k+1/2} - A_{i,j,k-1/2}\overline{\mathbf{F}}_{i,j,k-1/2}\right] \\ &+ \frac{\Delta t}{\alpha_{i,j,k}\Delta x\Delta y\Delta z}[\mathbf{C}+\mathbf{D}],\end{aligned} \tag{13}$$

where the friction term **D** represents the friction force at $\Gamma_{i,j,k}$ and is required to enforce the no-slip condition with respect to the interface-tangential velocity components at $\Gamma_{i,j,k}$. **C** is a momentum-exchange term which imposes the no-slip condition with respect to the normal velocity components at the interface. All terms on the right-hand-side of Eq. (13) are evaluated at time t^n. A more detailed description of these terms will be given below.

The face apertures, volume fractions and the interface segment (see Fig. 2) can be determined by any suitable approach. When the interface is represented by a zero-level-set contour many efficient approaches for calculating these quantities are possible. The use of a level-set field description allows for the treatment of arbitrary geometries and for a straightforward extension to moving interfaces. Empty cells, i.e. cells with zero fluid volume fraction and zero face apertures, are initialized with $\bar{\mathbf{u}} = 0$ and are left unmodified during time advancement for fluid–solid interaction problems.

2.2.2. Friction term **D**

The friction force on $\Gamma_{i,j,k}$ is accounted for by adding

$$\mathbf{D} = -\int_{\Gamma_{i,j,k}} \boldsymbol{\tau}\, dS \tag{14}$$

to the flux balance of Eq. (13). Similarly as in [29] we neglect velocity gradients in tangential direction because they are zero for rigid immersed boundaries. Furthermore the continuity condition Eq. (3) must be satisfied, so that the wall shear stress $\boldsymbol{\tau}$ can be expressed in a local frame of reference (see Fig. 3) as

$$\boldsymbol{\tau} = \nu(\nabla\bar{\mathbf{u}})\cdot\mathbf{n}_{\perp}, \tag{15}$$

using the kinematic viscosity ν Eq. (14) becomes

$$\mathbf{D} = -\int_{\Gamma_{i,j,k}} \nu(\nabla\bar{\mathbf{u}})\cdot\mathbf{n}_{\perp}\, dS. \tag{16}$$

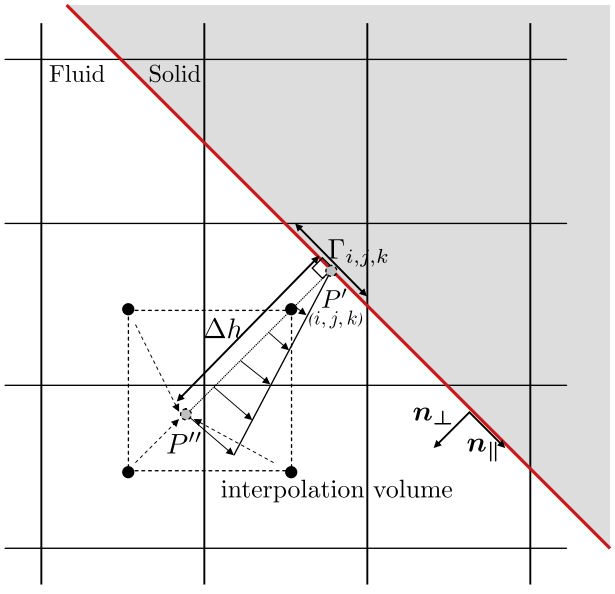

Fig. 3. Linear approximation of the velocity gradient of a velocity cell.

For a linear approximation of the wall-normal velocity gradient we use the difference of the interface velocity $\bar{\mathbf{u}}_\Gamma(P')$ and the tangential velocity $\bar{\mathbf{u}}_\parallel(P'')$ in point P'', see Fig. 3. The location of P'' is defined by moving from the foot point P' along the interface normal for a distance Δh. P' is the normal projection of the cell center of cell (i,j,k) on $\Gamma_{i,j,k}$. The velocity in P'' is calculated by trilinear Lagrangian interpolation from the velocities at the the eight neighboring velocity-cell centers. The final form of $\mathbf{D}$ is

$$\mathbf{D} = -\frac{\nu\Gamma_{i,j,k}}{\Delta h}\left(\bar{\mathbf{u}}_\parallel - \bar{\mathbf{u}}_\Gamma\right). \tag{17}$$

The velocity $\bar{\mathbf{u}}_\Gamma$ at the boundary is known and vanishes for non-moving boundaries. The distance Δh needs to be related to the cell volume, we set

$$\Delta h = 0.5\sqrt{(\Delta x \cdot n_{\perp,x})^2 + (\Delta y \cdot n_{\perp,y})^2 + (\Delta z \cdot n_{\perp,z})^2}. \tag{18}$$

Δx, Δy and Δz are the dimensions of the control volume (i, j, k) and $n_{\perp,x}$, $n_{\perp,y}$, $n_{\perp,z}$ are components of the normal vector on $\Gamma_{i,j,k}$. We note that the friction term in Eq. (13) can be extended in a straightforward way to include a wall model for turbulence [3].

2.2.3. Momentum-exchange term $\boldsymbol{C}$

For impermeable interfaces the interface normal velocity of the fluid equals that of the interface. In the following we assume for simplicity that the interface is impermeable and does not move so that the interface normal velocity $\bar{\mathbf{u}}_\perp = (\bar{\mathbf{u}} \cdot \mathbf{n}_\perp)\mathbf{n}_\perp$ vanishes. This is achieved with a pressure–velocity coupling term, which is required because some small cut cells do not contribute to the discrete Poisson equation on a staggered grid. More details will be given in Section 2.2.5. For small cells that do not contribute to the discrete Poisson equation we impose the zero-normal-velocity condition by

$$\mathbf{C} = -\bar{\mathbf{u}}_{\perp,i,j,k}\frac{V_{i,j,k}}{\Delta t}. \tag{19}$$

$\mathbf{C}$ is added to the flux balance in Eq. (13). A generalization to moving boundaries is straightforward.

2.2.4. Small cell treatment

Cut-cell methods, such as the one presented in this paper, can generate cells with a very small fluid volume fraction. A special treatment of such cells is necessary for numerical stability when excessively small time steps are to be avoided. For such purposes cell merging [62], cell linking [29], and mixed approaches [19] are reported in the literature. Cell merging requires to calculate additional fluxes with adjacent cells. Also, the formulation of merging algorithms in three dimensions tends to be cumbersome [29]. Cell linking can avoid such problems. However, due to various conditional operations, this approach appears less suitable for the treatment of moving boundaries.

In the present method, the fluid of the small cells is mixed with that of the neighboring cells. The approach of Hu et al. [26] is adapted for staggered grids in three dimensions. Target cells for mixing are determined from an evaluation of the normal vector $\mathbf{n}_\perp = [n_{\perp,x}, n_{\perp,y}, n_{\perp,z}]$. Different from the original approach [26] all next neighbor cells are included in the mixing procedure. Suppose (i,j,k) is a cut cell, we have three target cells in two dimensions, as shown in Fig. 4, and seven target cells in three dimensions. The conservative exchange between small cell (i,j,k) and their target cell in, e.g. x-direction, is calculated by

$$X^x = \frac{\beta^x_{i,j,k}}{\beta^x_{i,j,k}V_{i,j,k} + V_{tgt}}\left[V_{i,j,k}(Vq^\star)_{tgt} - V_{tgt}(Vq^\star)_{i,j,k}\right], \tag{20}$$

where tgt is the index of the target cell and $q^\star$ is the mixed conservative quantity. Terms for target cells in the other directions are formulated accordingly. $q^\star$ can be the flux divergence $\nabla \cdot \mathbf{F}$, the velocity or a scalar concentration. We found that mixing $\nabla \cdot \mathbf{F}$ results in a more accurate pressure approximation, see also Section 2.3. $\beta^x_{i,j,k}$ is the fraction of mixing with the target cell in x-direction. The mixing fractions $\beta_{i,j,k}$ are defined as

$$\begin{aligned}
\beta^x_{i,j,k} &= n^2_{\perp,x}\alpha^{x\gamma}_{tgt}, & \beta^y_{i,j,k} &= n^2_{\perp,y}\alpha^{y\gamma}_{tgt},\\
\beta^z_{i,j,k} &= n^2_{\perp,z}\alpha^{z\gamma}_{tgt}, & \beta^{xy}_{i,j,k} &= |n_{\perp,x}n_{\perp,y}|\alpha^{xy\gamma}_{tgt},\\
\beta^{xz}_{i,j,k} &= |n_{\perp,x}n_{\perp,z}|\alpha^{xz\gamma}_{tgt}, & \beta^{yz}_{i,j,k} &= |n_{\perp,y}n_{\perp,z}|\alpha^{yz\gamma}_{tgt},\\
\beta^{xyz}_{i,j,k} &= |n_{\perp,x}n_{\perp,y}n_{\perp,z}|^{2/3}\alpha^{xyz\gamma}_{tgt}.
\end{aligned} \tag{21}$$

These mixing fractions are normalized subsequently in order to satisfy

$$\beta^x_{i,j,k} + \beta^y_{i,j,k} + \cdots + \beta^{xyz}_{i,j,k} = 1. \tag{22}$$

The contributions of cells with large volume fraction are amplified by the integer power $\gamma \geqslant 1$. This leads to a stronger contribution for cells with a bigger volume fraction thus enhancing numerical stability. We use $\gamma = 5$ for all tests in this paper.

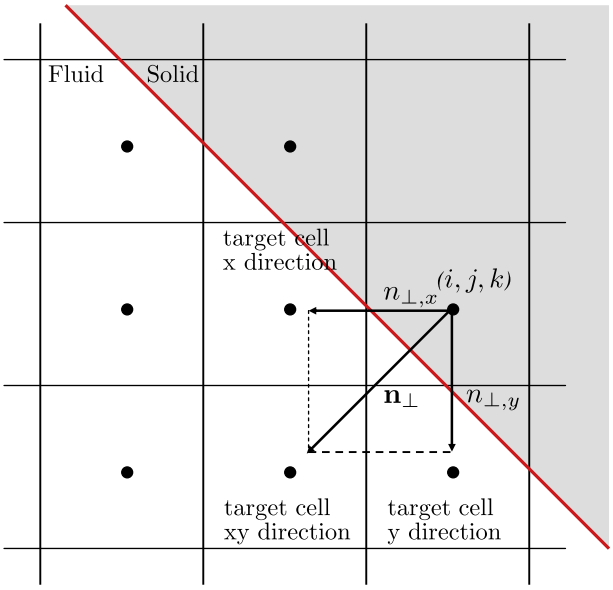

Fig. 4. Mixing procedure for the small fluid cell (i, j, k).

Note that conservation is ensured since each conservative quantity $M_{i,j,k}$ that a small cell obtains from a target cell corresponds to a loss M_{tgt} of the target cell.

$$M^x_{i,j,k} = X^x = -M^x_{tgt}. \tag{23}$$

Once the mixing exchanges are determined for all small cells the solution q is obtained by

$$q_{i,j,k} = q^\star_{i,j,k} + \frac{1}{V_{i,j,k}}\left(\sum M^x + \sum M^y + \ldots + \sum M^{xyz}\right), \tag{24}$$

where $q^\star$ is the solution before mixing (see also Section 2.3 for the algorithm). Since mixing is carried out before the final pressure projection, the solution after each time step is divergence free.

2.2.5. Homogeneous Neumann condition for pressure projection

To satisfy the incompressible continuity Eq. (3), a Poisson equation is solved for the pressure correction $\bar{\phi}$

$$\nabla^2\bar{\phi} = -\nabla\cdot\bar{\mathbf{u}}^\star_{i,j,k}. \tag{25}$$

For consistency it is necessary to use the same discrete gradient and divergence operators in the momentum equation and for Eq. (25). Using a staggered grid formulation, the velocities at the cell faces of the pressure cell are known, so that the discretized Poisson equation can be written as

$$\begin{aligned}
&\frac{1}{\Delta x}\left[A_{i+1/2,j,k}\frac{\partial\bar{\phi}}{\partial x}\Big|_{i+1/2,j,k} - A_{i-1/2,j,k}\frac{\partial\bar{\phi}}{\partial x}\Big|_{i-1/2,j,k}\right]\\
&+\frac{1}{\Delta y}\left[A_{i,j+1/2,k}\frac{\partial\bar{\phi}}{\partial y}\Big|_{i,j+1/2,k} - A_{i,j-1/2,k}\frac{\partial\bar{\phi}}{\partial y}\Big|_{i,j-1/2,k}\right]\\
&+\frac{1}{\Delta z}\left[A_{i,j,k+1/2}\frac{\partial\bar{\phi}}{\partial z}\Big|_{i,j,k+1/2} - A_{i,j,k-1/2}\frac{\partial\bar{\phi}}{\partial z}\Big|_{i,j,k-1/2}\right] - \frac{\alpha_{i,j,k}\Gamma_{i,j,k}r_{p,\Gamma}}{V_{i,j,k}}\\
&= -\frac{1}{\Delta x}\left[A_{i+1/2,j,k}\bar{u}^\star_{i+1/2,j,k} - A_{i-1/2,j,k}\bar{u}^\star_{i-1/2,j,k}\right]\\
&-\frac{1}{\Delta y}\left[A_{i,j+1/2,k}\bar{v}^\star_{i,j+1/2,k} - A_{i,j-1/2,k}\bar{v}^\star_{i,j-1/2,k}\right]\\
&-\frac{1}{\Delta z}\left[A_{i,j,k+1/2}\bar{w}^\star_{i,j,k+1/2} - A_{i,j,k-1/2}\bar{w}^\star_{i,j,k-1/2}\right] + \frac{\alpha_{i,j,k}\Gamma_{i,j,k}r_{u,\Gamma}}{V_{i,j,k}},
\end{aligned} \tag{26}$$

where $\bar{u}^\star$, $\bar{v}^\star$, $\bar{w}^\star$ are the intermediate velocities at the cell faces and $r_{u,\Gamma}$ and $r_{p,\Gamma}$ are the velocity and pressure interface condition at $\Gamma_{i,j,k}$. The pressure gradient is discretized with second order central differences. For non-moving boundaries we set $r_{u,\Gamma} = \bar{\mathbf{u}}_\Gamma^\star \cdot \mathbf{n}_\perp$ to zero. For imposing the homogeneous Neumann condition $\nabla\bar{\phi} \cdot \mathbf{n}_\perp = 0$ we set $r_{p,\Gamma} = 0$ at the interface. The interface treatment decouples the fluid domain from the interior of the obstacle. The discrete Poisson equation is solved for the fluid domain only. Note that very small cells do not contribute to Eq. (26). For such cells the momentum-exchange term Eq. (19) ensures zero wall-normal velocity. Eq. (26) can be written as a linear equation system

$$\mathbf{M}\bar{\phi} = \mathbf{b} \tag{27}$$

and solved for $\bar{\phi}$ using a standard procedure.

2.3. Implementation

At initialization of a computation a level-set field is determined on the basis of a geometry input. Cut cells are subsequently identified and their face apertures and volume fractions are determined. For non-moving immersed interfaces this procedure is applied once at the beginning of the computation. For moving interfaces, the level-set field is transported and indicates the evolution of time interface location. The extension to moving interfaces is straightforward and not further discussed in this paper. The general procedure for one Euler time step can be summarized as follows:

Step 1. The convective and diffusive fluxes are calculated for standard and cut cells in the same way.
Step 2. The fluxes across the cell faces of cut cells are scaled with the face apertures.
Step 3. Friction forces at the immersed interface are taken into account by adding **D** according to Eq. (17). **D** is added to the flux balance Eq. (13).
Step 4. The flux divergence is computed according to Eq. (13), where the volume fractions are required for a conservative formulation.
Step 5. The flux divergence of cells with a volume fraction $\alpha_{i,j,k} < 0.5$ is mixed with neighboring fluid cells of the immersed interface using the conservative mixing procedure, Eq. (24), with

$$q^\star_{i,j,k} = \frac{1}{V_{i,j,k}} \int_{\partial(V_{i,j,k} \cap \Omega)} \mathbf{F} \cdot \mathbf{n}_\perp \, dS.$$

Step 6. Zero wall-normal velocity for small cells is imposed by **C**, see Eq. (19), and added to Eq. (13).
Step 7. The prediction for the pressure gradient is added to mixed flux divergence and the intermediate solution $\bar{\mathbf{u}}^\star_{i,j,k}$ is computed.
Step 8. In the subsequent pressure correction, the Neumann condition for pressure is ensured by locally changing the coefficient matrix close to the immersed boundary, see also Eq. (26). The resulting velocity is divergence free.

At the end of this procedure, mass and momentum conservation are locally and globally ensured by construction. Mass conservation is ensured discretely according to the accuracy threshold chosen in the Poisson solver, up to machine precision if desired. Discrete conservation is monitored throughout a computation. A third-order Runge–Kutta time integration scheme [49] is used in this paper. In each Runge–Kutta sub-step, all the above steps are invoked once. Additionally, the mixing procedure is invoked for the solution after the first Runge–Kutta substep, which improves stability and allows for the use of CFL = 1 based on the full cell sizes. For moving interfaces the level-set field needs to be advanced in time. After each time step cut cells are identified with the instantaneous zero-level-set, and their face apertures and volume fractions are updated.

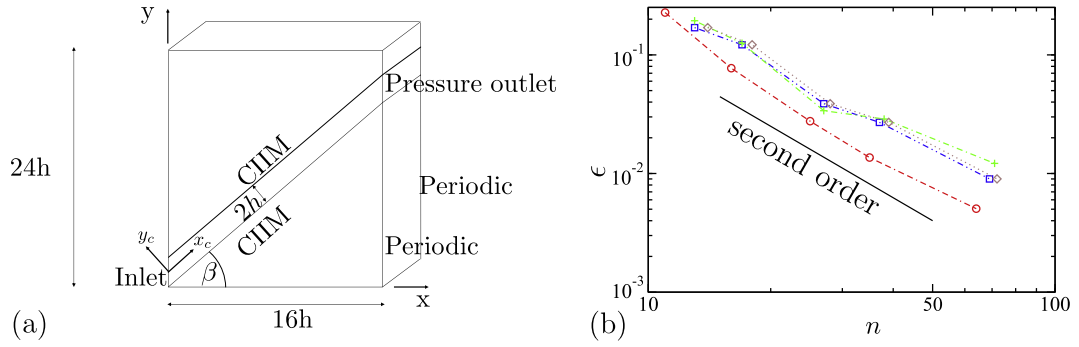

Fig. 5. (a) Computational set-up for the inclined channel flow at $Re = 20$ and (b) error for different grid resolutions and different inclination angles ($\cdot - - \circ$: $\beta = 20°$, $- \cdot\cdot \square$: $\beta = 30°$, $\cdot - \cdot +$: $\beta = 40°$, $\cdot\cdot\cdot \diamond$: $\beta = 50°$).

Table 1
Grids and number of computational cells over channel height n for the inclined channel flow at $Re = 20$.

$N_x \times N_y$	n_{20°	n_{30°	n_{40°	n_{50°
40×60	11	13	13	14
60×90	16	17	17	18
120×180	25	27	27	28
180×270	35	37	37	39
360×540	64	69	69	72

3. Validation results

In this section numerical examples are provided to illustrate the performance of the new method. All test cases are single-phase flows and have non-moving fluid–solid interfaces. For discretization in space ALDM is used for the convective terms, and a second-order accurate Central Difference Scheme (CDS) for the viscous terms and the pressure gradient. Note that for non-turbulent flow ALDM [21] recovers a central second-order finite-volume scheme. The proposed Conservative Immersed Interface Method (CIIM) can also be used with any other finite-volume discretization. Time advancement is performed using a third-order explicit three step Runge–Kutta scheme [49]. The pressure Poisson equation is solved using a Bi-Conjugate Gradient Stabilized (BiCGStab) iterative solver. All computations are carried out with a CFL number of 1.0 based on the full cells. The Reynolds number is defined as $Re = \frac{\rho_\infty U d}{\mu_\infty}$ where ρ_∞ is the reference density and μ_∞ is the reference dynamic viscosity. The reference velocity U and the reference length scale d as well as computational details for each case are given in the corresponding subsection.

3.1. Inclined channel flow at Re = 20

The first test case is the laminar flow through a plane channel that is inclined at $\beta = 20^\circ$, 30°, 40° and 50° with respect to the grid. Based on the channel half width h and the mean velocity U_b, the Reynolds number is $Re = 20$. This test case in particular validates the viscous term of CIIM. The computational domain is shown in Fig. 5(a).

The length of the channel is at least ten times the channel width. A parabolic velocity profile is defined at the inlet boundary with the velocity aligned parallel to the axis of the channel. At the outlet a pressure boundary condition is imposed. In spanwise direction periodic boundary condition are used. At the walls of the channel, the no-slip condition is imposed by CIIM.

The order of accuracy is determined from error estimates for the velocity profiles on six successively refined equidistant grids, see Table 1. N_x and N_y are the number of points in the respective direction of the computational domain.

To compute the error, the following equation is applied to the compare the velocity profile of the computations with the analytical profile at half the channel length

$$\epsilon = \left(\frac{1}{n} \sum_{r=1}^{n} (u_r^{numerical} - u_r^{analytical})^2 \right)^{1/2}, \tag{28}$$

where n is the total number of points across the channel. In Fig. 5(a) the error of the velocity profile with respect to the analytical profile for the different grid resolutions and inclination angles is shown. For all inclination angles the error decreases with about second-order. CIIM is compared with a simple blocking method [24] in Fig. 6(a). The blocking method shows a

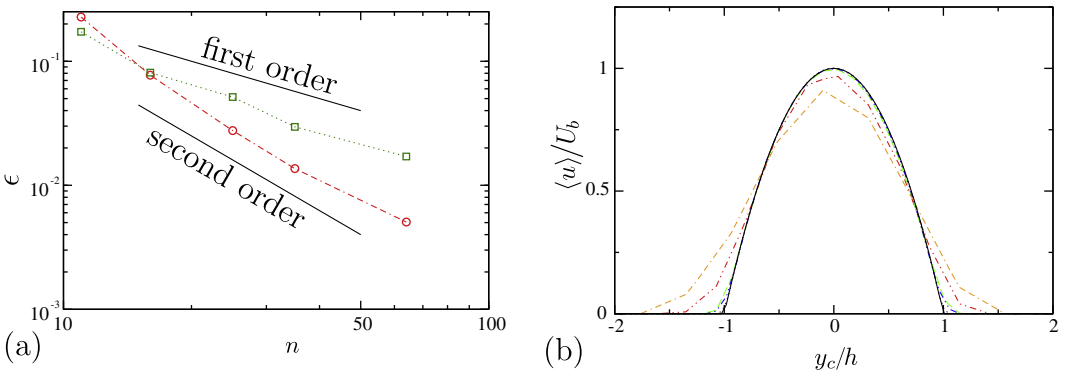

Fig. 6. (a) Error for different grid resolutions with an inclination angle $\beta = 20^\circ$ for CIIM and for the blocking method (·−−○: with CIIM, ···□: with blocking method) and (b) streamwise velocity profiles for the inclined channel flow at $\beta = 20^\circ$ with CIIM for different grid resolutions (·−−: $n = 11$, −··: $n = 16$, −−: $n = 25$, ·−·: $n = 35$, ···: $n = 64$, —: analytical profile).

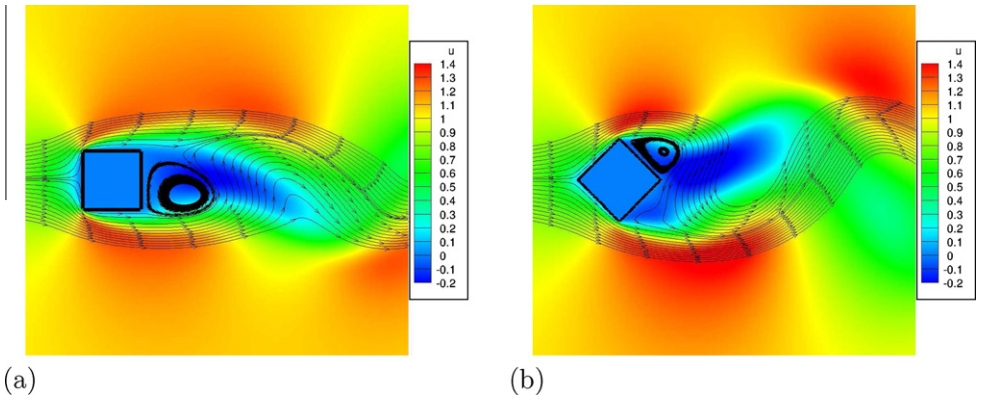

Fig. 7. (a) Streamwise velocity and streamlines for the flow over a non-inclined square cylinder and (b) 45°-inclined square cylinder at $Re = 100$.

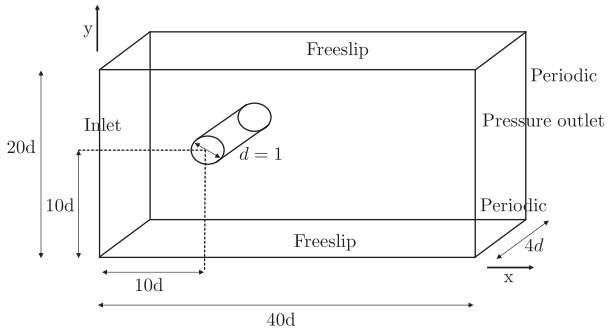

Fig. 8. Computational set-up for the flow over a cylinder at different Reynolds numbers.

Table 2
Inclination angle, drag coefficient, maximum lift coefficient, root-mean-square lift coefficient and Strouhal number for the flow over a non-inclined and 45°-inclined square cylinder at $Re = 100$.

Study	α (°)	C_D	$C_{L,max}$	$C_{L,rms}$	St
Okajima [40], experiment	0	–	–	–	0.149
Davis and Moore [8], simulation	0	1.63	–	–	0.152
Franke et al. [12], simulation	0	1.61	0.27	–	0.154
Sohankar et al. [50], simulation	0	1.48	–	0.18	0.150
Present, simulation ($n = 76$)	0	1.57	0.27	0.19	0.151
Sohankar et al. [50], simulation	45	1.72	–	0.48	0.182
Present, simulation ($n = 79$)	45	1.76	–	0.49	0.184

higher error than CIIM and only first-order convergence. In Fig. 6(b) the velocity profiles with CIIM for different grid resolutions are compared with the analytical profile for $\beta = 20°$. The highest error occurs at the immersed interface and amounts to 1–2% in the first full fluid cell on the fine grid ($n = 64$) in normal direction of the interface. Already for moderate resolutions the global agreement with the analytical solution is good.

3.2. Flow over a square cylinder at Re = 100

Two square cylinder cases are investigated: (a) the non-inclined square cylinder (see Fig. 7(a)) and (b) a square cylinder inclined by $\alpha = 45°$ with respect to the incoming flow (see Fig. 7(b)). At Reynolds number $Re = 100$ based on the projected cylinder width d in the streamwise direction and the free stream velocity U_∞ the flow over a square cylinder is unsteady, two-dimensional and laminar. The computational set-up used for all cylinder flow computations follows that of Fig. 8. Note that for both cases the cylinder boundaries do not coincide with grid lines.

3.2.1. Non-inclined square cylinder

Vortex shedding occurs at a Strouhal number $St = \frac{fd}{U_\infty} = 0.151$, where f is the shedding frequency. This finding agrees well with the experiments conducted by Okajima [40]. The Strouhal number, the time-averaged drag coefficient per unit length

Table 3
Grids and number of computational cells n over the projected cylinder width for the flow over a non-inclined and 45°-inclined square cylinder at $Re = 100$.

$N_x \times N_y$	$n_{0°}$	$n_{45°}$
128×64	15	17
192×96	23	25
256×128	34	36
384×192	51	53
512×256	76	79

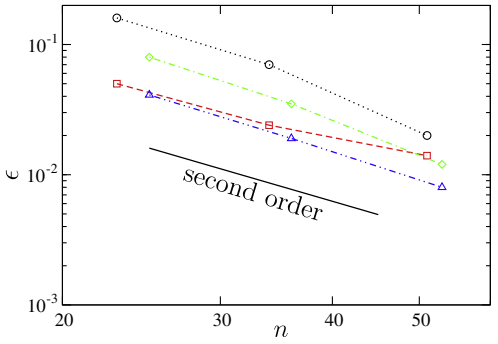

Fig. 9. Error in C_D ($\cdots\circ$) and $C_{L,max}$ ($--\square$) for the flow over a non-inclined square cylinder and error in C_D ($-\cdot-\cdot\diamond$) and $C_{L,rms}$ ($-\cdots\triangle$) for the flow over a 45°-inclined square cylinder at $Re = 100$ calculated on different grids.

$C_D = 2\frac{F_D}{\rho U_\infty^2 d}$ and the maximum lift coefficient per unit length $C_L = 2\frac{F_L}{\rho U_\infty^2 d}$ are compared with results from the literature in Table 2. F_D and F_L are the forces in streamwise and transverse direction. The mean drag force F_D of the cylinder consists of the friction force $F_{D,f}$ and the pressure force $F_{D,p}$ acting in the streamwise direction at the immersed interface. $F_{D,f}$ is determined by integrating the streamwise component of the friction term **D**, see Eq. (17), over all cut cells. For $F_{D,p}$, we integrate the pressure force over all cut cells. Accordingly, the maximum lift force F_L consists of $F_{L,p}$ and $F_{L,f}$. The Strouhal number for this and the following cylinder cases is determined from a Fourier transform of a velocity time signal obtained in the wake of the cylinder. The lift coefficient agrees very well with the simulation by Franke et al. [12], whereas the drag coefficient of our calculation is slightly lower. However, the difference is well within the range of variation for numerical and experimental data reported in literature [60].

To determine the grid-convergence order of CIIM also for this test case, the drag and lift coefficient have been calculated on five grids not aligned with the cylinder, with different resolutions and the same domain size. All grids are refined according to a hyperbolic tangent function centered around the *xz*-, *yz*-symmetry planes of the cylinder. Grid parameters are summarized in Table 3. The error is calculated with respect to the solution on the finest grid. In Fig. 9 we show a double-logarithmic plot of the errors for C_D and $C_{L,max}$. n is the number of points over the projected cylinder width. The plot shows that the error decreases with about second-order.

3.2.2. 45°-Inclined square cylinder

This test case is useful to determine also the accuracy of the geometry representation by the level-set. The same grids are used as for the non-inclined case (see Table 3). The Strouhal number, the time-averaged drag coefficient per unit length $C_D = 2\frac{F_D}{\rho U_\infty^2 d}$ and the root-mean-square lift coefficient per unit length $C_{L,rms} = 2\frac{F_{L,rms}}{\rho U_\infty^2 d}$ of our calculation are compared to the results of Sohankar et al. [50] in Table 2. The simulations of Sohankar et al. have been carried out on body-fitted grids. The agreement with our results is good, which gives direct evidence of the accuracy of the level-set description. The grid-convergence order is determined with the grids shown in Table 3. In Fig. 9 we show a double-logarithmic plot of the errors for C_D and $C_{L,rms}$. n is the number of points over the projected cylinder width. Note that about second-order convergence rate is achieved also for the inclined square cylinder.

3.3. Flow over a circular cylinder at Re = 40, Re = 100 and Re = 3900

In the following examples we consider the flow over a circular cylinder for a wide range of Reynolds numbers according to the set-up in Fig. 8. The circular cylinder is a standard configuration for testing immersed boundary and immersed interface methods and a huge amount of reference data are available from literature. The Reynolds number for all cases is based on the cylinder diameter d and the free stream velocity U_∞.

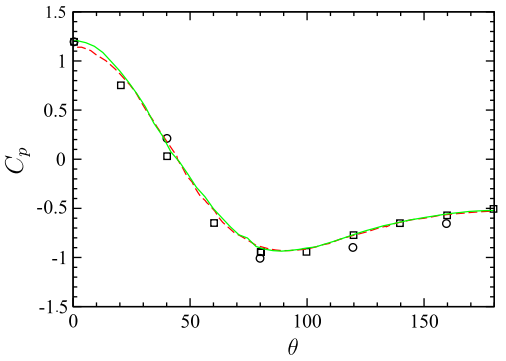

Fig. 10. Pressure coefficient C_p along the surface of a circular cylinder at $Re = 40$ ($\theta = 0$ in the stagnation point; □: experimental data Grove et al. [17], ∘: experimental data Thom [53], – –: Dröge [11], —: present method).

Table 4
Drag coefficient, pressure drag coefficient, separation angle and recirculation bubble length for the flow over a circular cylinder at $Re = 40$.

Study	C_D	$C_{D,p}$	$C_{D,f}$	θ_{sep} (°)	L_r/d
Tritton [54], experiment	1.58	–	–	–	–
Grove et al. [17], experiment	–	0.92	–	137.2	–
Coutanceau and Bouard [7], experiment	–	–	–	126.5	2.13
Dennis and Chang [9], simulation	1.52	0.99	0.524	126.2	2.35
Ye et al. [62], simulation	1.52	–	–	–	2.27
Dröge [11], simulation	1.58	1.02	0.56	126.67	2.22
Present, simulation ($n = 72$)	1.56	1.04	0.52	134.6	2.28

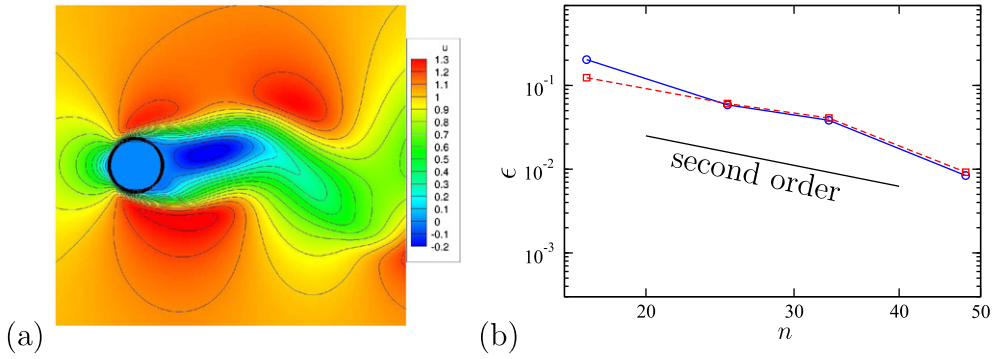

Fig. 11. (a) Streamwise velocity and contour lines for the flow over a circular cylinder at $Re = 100$. (b): error in C_D (– –□) and C_L(—∘) for the flow past a circular cylinder at $Re = 100$ calculated on different grids.

3.3.1. Flow over a circular cylinder at Re = 40

At $Re = 40$ laminar separation occurs and exhibits a two-dimensional symmetric wake. The calculation is carried out on a locally refined grid close to the immersed boundary with a total number of 175,000 computational cells and 72 computational cells along the cylinder diameter. The surface pressure coefficient $C_p = 2\frac{p-p_\infty}{\rho U_\infty^2}$ is compared in Fig. 10 with experimental and numerical results. p_∞ is measured at the inlet plane.

The drag, the separation angle and the length of the recirculation bubble compare well with reference data from experiments and other simulations, in Table 4. We also note the good agreement for the individual contributions of pressure and friction to the drag coefficient.

3.3.2. Flow over a circular cylinder at Re = 100

At $Re = 100$ the flow is unsteady, two-dimensional and laminar. For CIIM flow separation occurs at a an angle of 119° measured from the stagnation point, see Fig. 11(a). Vortex shedding occurs at $St = 0.165$. A comparison of C_D, C_L and St with our results experimental and numerical results is given in Table 5, which shows that our results are well within the range reported in the literature.

Table 5
Drag coefficient, maximum lift coefficient, separation angle and Strouhal number for the flow over a circular cylinder at $Re = 100$.

Study	C_D	$C_{L,max}$	θ_{sep} (°)	St
Tritton [54], experiment	1.26	–	–	–
Henderson [20], experiment	1.3	–	122	–
Fey et al. [16], experiment	–	–	–	0.165
Kim et al. [30], simulation	1.33	0.32	–	0.165
Dröge [11], simulation	1.24	0.30	117	0.165
Present, simulation ($n = 76$)	1.26	0.34	119	0.165

Table 6
Grids and number of computational cells n along the diameter for the flow over a circular cylinder at $Re = 100$.

$N_x \times N_y$	n
128×64	15
192×96	23
256×128	34
384×192	51
512×256	76

We have also analyzed the influence of the amount of mixing, i.e. the effect of the mixing threshold α_{crit}, on the accuracy of the solution. A variation of the small-cell mixing criterion down to $\alpha_{crit} = 0.2$ leads to a decrease of 0.9% for the drag coefficient and a variation up to $\alpha_{crit} = 0.7$ to an increase of 1.6% with respect to the CIIM-standard solution. The amount of mixing was chosen as best compromise between accuracy and overall efficiency and does not significantly affect the computed flow field.

For a convergence study calculations have been performed on five grids with different resolution. All grids have been refined according to a tangent hyperbolic function centered at the xz-, yz-symmetry planes of the cylinder. The different grid resolutions are summarized in Table 6, where the finest grid is taken as reference for the error estimation. For C_D and $C_{L,max}$ we find second-order accuracy, see Fig. 11(b).

3.3.3. Flow over a circular cylinder at Re = 3900

At $Re = 3900$ the unsteady wake is turbulent. Within the turbulent wake the subgrid-scale modeling capacity of ALDM is employed. Calculations were done on a locally refined grid with a total of 7 million cells (see Fig. 12). The cell size of all cells at the immersed interface is $\Delta x = \Delta y = 0.0025/d$, so that the resolution is similar to the LES of Franke and Frank [13] and Fröhlich [14]. The first computational cell in the wall-normal direction is within the viscous sublayer of the cylinder. The local mesh refinement algorithm is based on ghost cells in the grid transition regions. Data are assigned to ghost cells by a

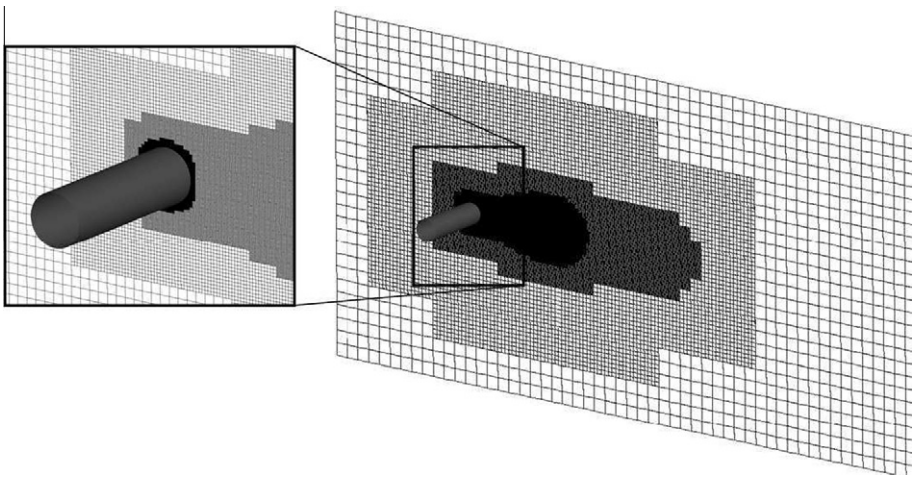

Fig. 12. Locally refined grid for flow over circular at $Re = 3900$.

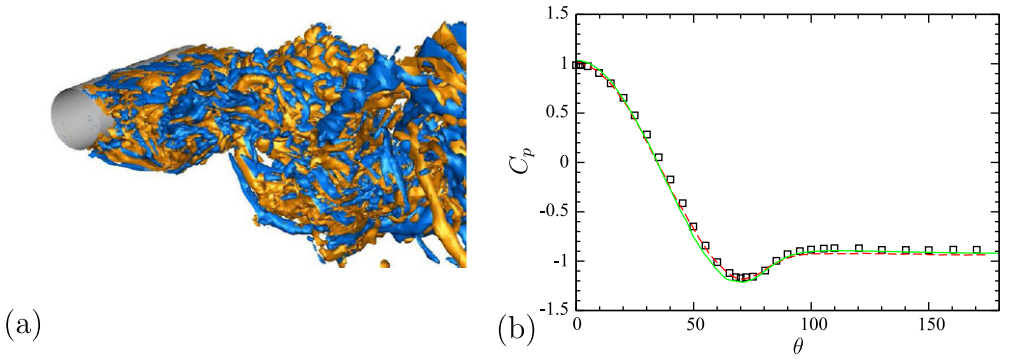

Fig. 13. (a) Streamwise vorticity-isosurface ±1.5 s^{-1} for the flow over circular cylinder at $Re = 3900$. (b) Pressure coefficient C_p along the surface of a circular cylinder at $Re = 3900$ ($\theta = 0$ in the stagnation point; □: experimental data Norberg extracted from Kravchenko and Moin [31], – –: Kravchenko and Moin [31], —: present method).

third-order conservative interpolation scheme. This scheme ensures mass and momentum conservation. The computational stencil does not change at grid transition. All cut cells are on the finest grid level.

Fig. 13(a) gives an impression of the instantaneous turbulent wake behind the cylinder. A good qualitative agreement is observed with Refs. [14,31].

For a quantitative validation, turbulence statistics are sampled over 50 shedding cycles after steady vortex shedding was established. The results are compared with the pressure measurements of Norberg extracted from Kravchenko and Moin [31], hot-wire measurements of Ong and Wallace [41], the particle-image velocimetry (PIV) data of Lourenco and Shih [33], the hot-wire measurements and particle-image velocimetry data of Parnaudeau et al. [42], and the LES of Kravchenko and Moin [31].

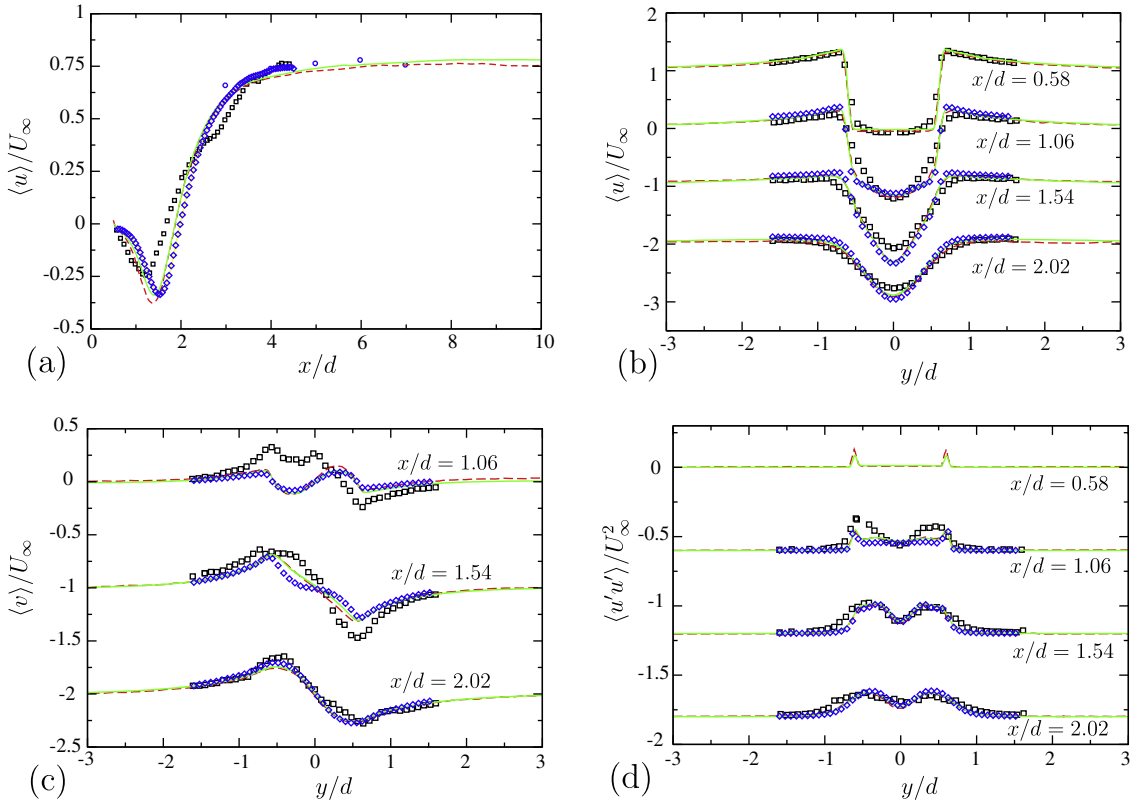

Fig. 14. (a) Mean streamwise velocity on the centerline of the cylinder, (b) mean streamwise velocity, (c) mean transverse velocity and (d) streamwise velocity fluctuations at different locations in the wake of a circular cylinder at $Re = 3900$ (□: experimental data Lourenco and Shih [33], ○: experimental data of Ong and Wallace [41], ◇: experimental data Parnaudeau et al. [42], – –: LES of Kravchenko and Moin [31] and —: present method).

Table 7
Drag coefficient, bulk suction coefficient, separation angle, recirculation bubble length and Strouhal number for the flow over a circular cylinder at $Re = 3900$.

Study	C_D	$C_{p,b}$	θ_{sep} (°)	L_r/d	St
Cardell taken from [35], experiment	–	–	–	1.33	0.215
Norberg taken from [31], experiment	0.98	−0.9	–	–	0.21
Lourenco and Shih [33], experiment	0.99	–	86	1.19	0.215
Ong and Wallace [41], experiment	–	–	–	–	0.21
Parnaudeau et al. [42], experiment	–	–	–	1.51	0.208
Dröge [11], simulation	1.01	−0.88	87.7	1.26	0.210
Franke and Frank [13], simulation	0.98	−0.85	88.2	1.64	0.209
Fröhlich et al. [14], simulation	1.08	−1.03	88.1	1.09	0.216
Kravchenko and Moin [31], simulation	1.04	−0.94	88	1.35	0.210
Present, simulation	1.05	−0.92	88	1.38	0.210

The pressure coefficient C_p shows good agreement with the experimental results of Norberg and numerical results of Kravchenko and Moin, see Fig. 13(b). The mean streamwise velocity along the centerline is shown in Fig. 14(a). Our LES shows a good agreement of the near wake with the simulation by Kravchenko and Moin and the PIV experiments of Parnaudeau et al. [42]. Neither our results nor that of Kravchenko and Moin reproduce the dip at $x/d = 3$. Mean velocity profiles are shown in Fig. 14(b) and (c), and the Reynolds normal stresses $\langle u'u' \rangle / U_\infty^2$ are shown in Fig. 14(d). Again our results agree well with the simulation of Kravchenko and Moin [31] and the PIV data of Parnaudeau et al. [42] for the near wake so that a good performance of the CIIM can be claimed.

We compare the mean drag coefficient, bulk suction coefficient, mean separation angle, mean recirculation length and Strouhal number with the literature, in Table 7. All quantities are found to be well in the range of experimental data and results of previous DNS and LES computations. In this test case, the computational cost for CIIM and the flux calculation with ALDM, each amounts to 2% of the overall computational time, while the Poisson solver needs about 80%.

3.3.4. Turbulent channel flow with periodic constrictions at Re = 10,595

The incompressible turbulent flow in a channel with a periodic arrangement of smooth constrictions is calculated at $Re = 10{,}595$ based on the constriction height h and bulk velocity U_b above the constriction. ALDM is employed as subgrid-scale model. The dimensions of the computational domain and the boundary conditions are shown in Fig. 15. A fixed Reynolds number and constant mass flux is ensured by a volume force term in the Navier–Stokes equations. A total number

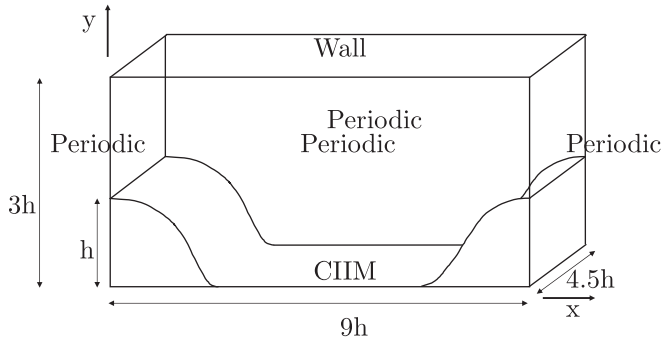

Fig. 15. Computational set-up for the flow over periodic hills at $Re = 10{,}595$.

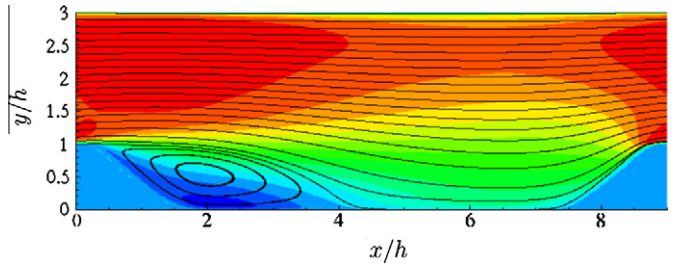

Fig. 16. Contour lines of the mean streamwise velocity for the flow over periodic hills at $Re = 10{,}595$.

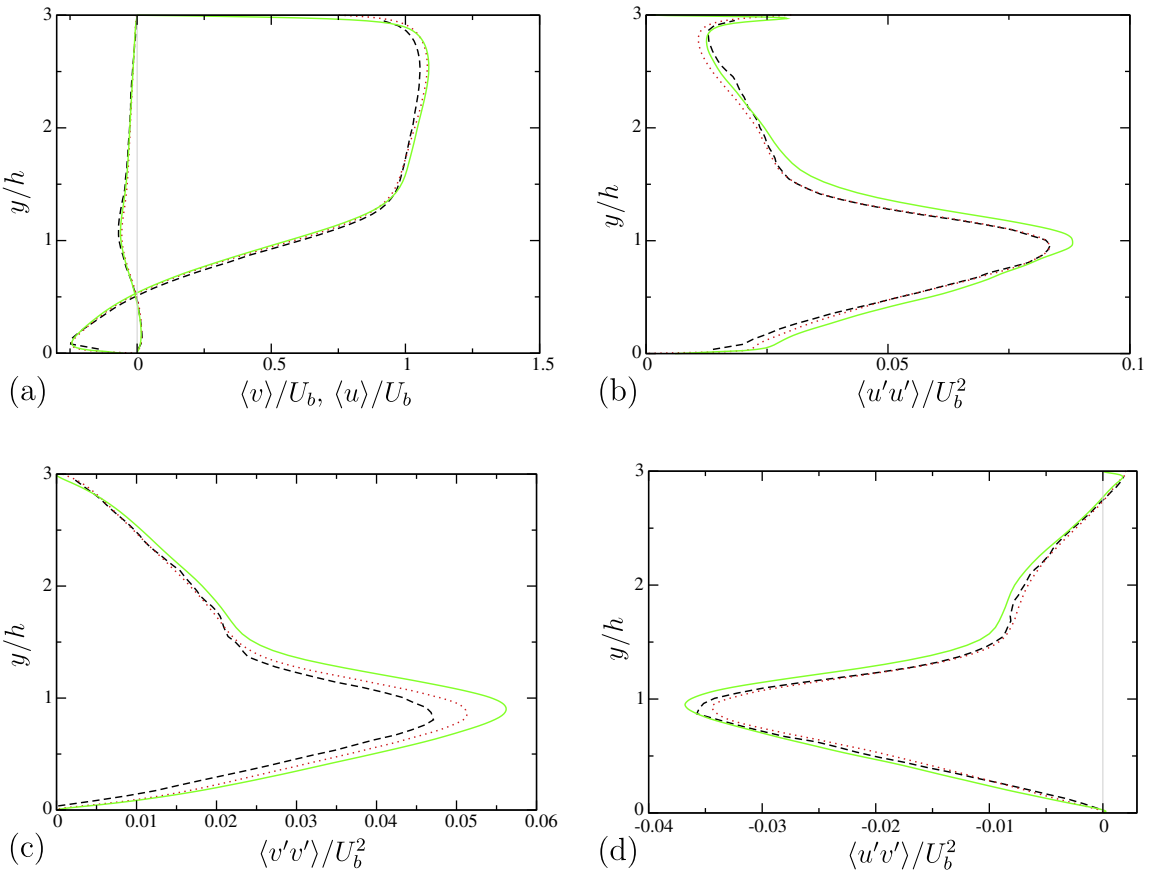

Fig. 17. (a) Mean streamwise and cross flow velocity, (b) streamwise velocity fluctuations, (c) cross flow velocity fluctuations and (d) shear stress at $x/h = 2$ for the flow over periodic hills at $Re = 10{,}595$ (– –: experiment [47], ⋯: well-resolved LES on a grid with 13×10^6 cells [2], —: present method).

of 1.6 million cells are used: $192 \times 128 \times 64$ (streamwise $\times$ wall-normal $\times$ spanwise). The grid is stretched in streamwise and wall-normal direction to resolve the crest with $\Delta x_{crest}/h = 0.0375$ and $\Delta y_{crest}/h = 0.0051$ comparable to Refs. [2,24]. Top and bottom wall are resolved with $\Delta y/h = 0.008$ in wall normal direction. In spanwise direction the grid is equidistant with $\Delta z/h = 0.0703$.

At this considered Reynolds number the flow evolution is dominated by the detached shear layer above the unsteady recirculation zone. Fig. 16 gives an impression of the mean flow field. A good qualitative agreement is observed with Refs. [2,24].

For a quantitative validation, turbulence statistics are sampled over 25 flow-through times and averaged in the homogeneous spanwise direction. The results are compared with the experimental data of Rapp [47] and the well-resolved LES of Breuer et al. [2]. Breuer et al. used a dynamic Smagorinsky subgrid-scale model and a grid with 13 million cells. We show results for two stations, in the main recirculation region at $x/h = 2$ in Fig. 17, and behind the separation region in the reattached flow at $x/h = 6$ in Fig. 18. Overall, a good agreement for the mean flow and second-order statistics with reference data [2,47,24] is observed. In this test case, CIIM consumes 3% of the overall computational time, the flux calculation with ALDM 8% and the Poisson solver 81%.

4. Conclusion

In this paper we have developed a second-order Conservative Immersed Interface Method (CIIM) for Cartesian finite-volume discretizations of the incompressible Navier–Stokes equations. The method is applicable to any underlying finite-volume discretization. A zero-level-set contour represents the interface, which also allows to handle topological changes naturally. CIIM operates on fluxes of cut cells only and therefore ensures mass and momentum conservation. Friction forces on the immersed interface are accounted for by a friction term. The boundary condition of the normal velocity is satisfied by a momentum-exchange term and by imposing a homogeneous Neumann condition in the pressure projection. To ensure numerical stability a conservative mixing procedure is employed. Numerical validation examples demonstrate second-order

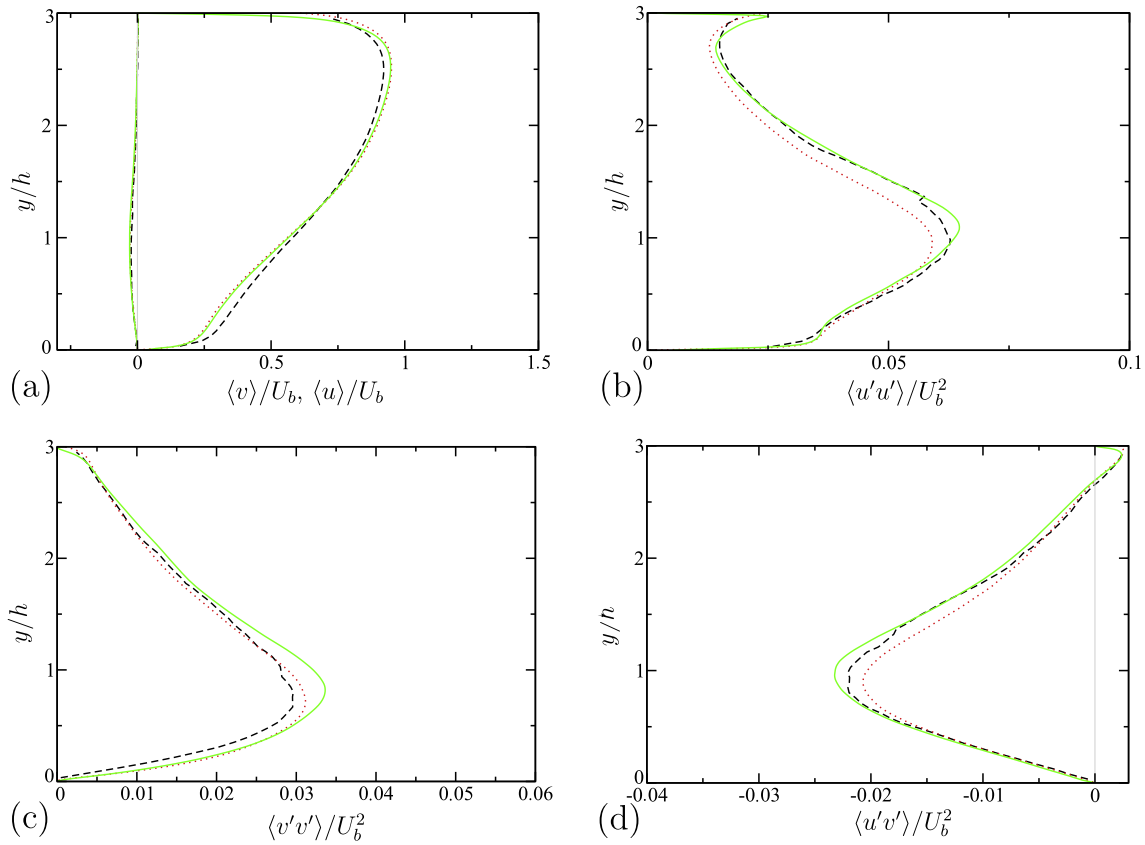

Fig. 18. (a) Mean streamwise and cross flow velocity, (b) streamwise velocity fluctuations, (c) cross flow velocity fluctuations and (d) shear stress at $x/h = 6$ for the flow over periodic hills at $Re = 10{,}595$ (– –: experiment [47], ⋯: well-resolved LES on a grid with 13×10^6 cells [2], —: present method).

convergence and good agreement with experimental and numerical reference data from literature. Discrete mass and momentum conservation, simple representation of the immersed interface and second-order convergence make CIIM a suitable method for representing non-moving and moving boundaries in turbulent flow computations.

Acknowledgements

The research was founded by the Deutsche Forschungsgemeinschaft. Computational resources have been provided by the Leibniz Rechenzentrum Munich. The first author is member of the Technische Universität München (TUM) Graduate School.

References

[1] J.B. Bell, P. Colella, H.M. Glaz, A second-order projection method for the incompressible Navier–Stokes equations, J. Comput. Phys. 85 (1989) 257–283.
[2] M. Breuer, N. Peller, Ch. Rapp, M. Manhart, Flow over periodic hills – numerical and experimental study in a wide range of Reynolds numbers, Int. J. Comput. Fluids 38 (2) (2009) 433–457.
[3] Z. Chen, A. Devesa, M. Meyer, S. Hickel, E. Lauer, C. Stemmer, N.A. Adams, Wall modelling for implicit large eddy simulation of favourable and adverse pressure gradient flows, in: Proceedings of the WALLTURB Workshop Progress in Wall Turbulence – Understanding and Modelling, Lille, 2009.
[4] M.-H. Chung, Cartesian cut cell approach for simulating incompressible flows with rigid bodies of arbitrary shape, Comput. Fluids 35 (2006) 607–623.
[5] D. Clarke, M. Salas, H. Hassan, Euler calculations for multi-element airfoils using Cartesian grids, AIAA J. 24 (3) (1986) 353–358.
[6] P. Colella, D. Graves, D. Modiano, E.G. Puckett, M. Sussman, An embedded boundary/volume of fluid method for free surface flows in irregular geometries, in: Proceedings of the FEDSM99, 3rd ASME/JSME Joint Fluids Engineering Conference, 1999.
[7] M. Coutanceau, R. Bouard, Experimental determination of the main features of the viscous flow in the wake of a circular cylinder in uniform translation. Part 1. Steady flow, J. Fluid Mech. 79 (1977) 231–256.
[8] R.M. Davis, E.F. Moore, A numerical study of vortex shedding from rectangles, J. Fluid Mech. 116 (1982) 475–506.
[9] S.C.R. Dennis, G. Chang, Numerical solutions for steady flow past a circular cylinder at Reynolds numbers up to 100, J. Fluid Mech. 42 (1970) 471–489.
[10] M. Dröge, R.W.C.P. Verstappen, A new symmetry-preserving Cartesian-grid method for computing flow past arbitrarily shaped objects, Int. J. Numer. Methods Fluids 47 (2005) 979–985.
[11] M. Dröge, Cartesian Grid Methods for Turbulent Flow Simulation in Complex Geometries, Ph.D thesis, University of Groningen, 2007.
[12] R. Franke, W. Rodi, B. Schönung, Numerical calculation of laminar vortex shedding flow past cylinders, J. Wind. Eng. Ind. Aerod. 35 (1990) 237–257.
[13] J. Franke, W. Frank, Large eddy simulation of the flow past a circular cylinder at $Re_D = 3900$, J. Wind Eng. Ind. Aerod. 90 (2002) 1191–1206.
[14] J. Fröhlich, W. Rodi, Ph. Kessler, S. Parpais, J.P. Bertoglio, D. Laurence, Large eddy simulation of flow around circular cylinders on structured and unstructured grids, CNRS DFG Collaborative Research Programme, vol. 66, Vieweg, Braunschweig, 1998, pp. 319–338.

[15] J.H. Ferziger, M. Peric, Computational Method for Fluid Dynamics, Springer Verlag, New York/Berlin, 1996.
[16] U. Fey, M. König, H. Eckelmann, A new Strouhal–Reynolds-number relationship for the circular cylinder in the range $47 < Re < 2 \cdot 10^5$, Phys. Fluids 10 (1998) 1547.
[17] A.S. Grove, F.H. Shair, E.E. Petersen, A. Acrivos, An experimental investigation of the steady separated flow past a circular cylinder, J. Fluid Mech. 19 (1964) 60–80.
[18] B. Griffith, C.S. Peskin, On the order of accuracy of the immersed boundary method: higher order convergence rates for sufficiently smooth problems, J. Comput. Phys. 208 (2005) 75105.
[19] D. Hartmann, M. Meinke, W. Schröder, An adaptive multilevel multigrid formulation for Cartesian hierarchical grid methods, Comput. Fluids 37 (2008) 1103–1125.
[20] R.D. Henderson, Details of the drag curve near the onset of vortex shedding, Phys. Fluids 7 (1995) 2102–2104.
[21] S. Hickel, N.A. Adams, J.A. Domaradzki, An adaptive local deconvolution method for implicit LES, J. Comput. Phys. 213 (2006) 413–436.
[22] S. Hickel, N.A. Adams, N.N. Mansour, Implicit subgrid-scale modeling for large-eddy simulation of passive-scalar mixing, Phys. Fluids 19 (2007) 095102.
[23] S. Hickel, N.A. Adams, On implicit subgrid-scale modeling in wall-bounded flows, Phys. Fluids 19 (2007) 105106.
[24] S. Hickel, T. Kempe, N.A. Adams, Implicit large-eddy simulation applied to turbulent channel flow with periodic constrictions, Theor. Comput. Fluid Dyn. 22 (2007) 227–242.
[25] S. Hickel, N.A. Adams, Implicit LES applied to zero-pressure-gradient and adverse-pressure-gradient boundary-layer turbulence, Int. J. Heat Fluid Flow 29 (2008) 626–639.
[26] X.Y. Hu, B.C. Khoo, N.A. Adams, F.L. Huang, A conservative interface method for compressible flows, J. Comput. Phys. 219 (2006) 553–578.
[27] H. Johannsen, P. Colella, A Cartesian grid embedded boundary method for Poisson's equation on irregular domains, J. Comput. Phys. 147 (1998) 60–85.
[28] S. Kang, G. Iaccarino, P. Moin, Accurate immersed-boundary reconstructions for viscous flow simulations, AIAA J. 47 (7) (2009) 1750–1760.
[29] M. Kirkpatrick, S. Armfield, J. Kent, A representation of curved boundaries for the solution of the Navier–Stokes equations on a staggered three-dimensional Cartesian grid, J. Comput. Phys. 184 (2003) 1–36.
[30] J. Kim, D. Kim, H. Choi, An immersed-boundary finite-volume method for simulations of flow in complex geometries, J. Comput. Phys. 171 (2001) 132–150.
[31] A. Kravchenko, P. Moin, Numerical studies of flow over a circular cylinder at $Re_D = 3900$, Phys. Fluids 12 (2000) 403–417.
[32] M. Lai, C.S. Peskin, An immersed boundary method with formal second-order accuracy and reduced numerical viscosity, J. Comput. Phys. 160 (2000) 705–719.
[33] L.M. Lourenco, C. Shih, Characteristics of the Plane Turbulent Near Wake of a Circular Cylinder, A Particle Image Velocimetry Study, Unpublished results, data extracted from Dröge [11].
[34] A. Mark, B.G.M. van Wachem, Derivation and validation of a novel implicit second-order accurate immersed boundary method, J. Comput. Phys. 227 (2008) 6660–6680.
[35] R. Mittal, Progress on LES of flow past a circular cylinder, in: Annual Research Briefs, Center for Turbulence Research, Stanford University, 1996, pp. 233–241.
[36] R. Mittal, Y. Utturkar, H.S. Udaykumar, Computational modeling and analysis of biomimetic flight mechanisms, AIAA J. (2002). 2002-0865.
[37] R. Mittal, V. Seshadri, H.S. Udaykumar, Flutter, tumble and vortex induced autorotation, Theor. Comp. Fluid Dyn. 17 (3) (2004) 16570.
[38] R. Mittal, G. Iaccarino, Immersed boundary methods, Annu. Rev. Fluid Mech. 37 (2005) 239–261.
[39] J. Mohd-Yusof, Combined Immersed-Boundary/B-Spline Methods for Simulations of Flow in Complex Geometries, CTR Annual Research Briefs, NASA Ames/Stanford University, 1997.
[40] A. Okajima, Strouhal numbers of rectangular cylinders, J. Fluid Mech. 123 (1982) 379–398.
[41] L. Ong, J. Wallace, The velocity field of the turbulent very near wake of a circular cylinder, Exp. Fluids 20 (1996) 441–453.
[42] P. Parnaudeau, J. Carlier, D. Heitz, E. Lamballais, Experimental and numerical studies of the flow over a circular cylinder at Reynolds number 3900, Phys. Fluids 20 (2008) 085101.
[43] N. Peller, A. Le Duc, A. Tremblay, M. Manhart, High-order stable interpolations for immersed boundary methods, Int. J. Numer. Methods Fluids 52 (2006) 1175–1193.
[44] C.S. Peskin, Flow Patterns Around Heart Valves: A Digital Computer Method for Solving the Equations of Motion, Ph.D. Thesis, Physiol. Albert Einstein Coll. Med., Univ. Microfilms, 378, 1972, pp. 72–30.
[45] C.S. Peskin, Numerical analysis of blood flow in the heart, J. Comput. Phys. 25 (1977) 220.
[46] C.S. Peskin, The immersed boundary method, Acta Numer. 2002 (2002) 1–39.
[47] C. Rapp, Experimentelle Studie der Turbulenten Strömung Ueber Periodische Hügel, Ph.D. Thesis, Technische Universitt Mnchen, 2008.
[48] A. Roma, C.S. Peskin, M. Berger, An adaptive version of the immersed boundary method, J. Comput. Phys. 153 (1999) 509–534.
[49] C.-W. Shu, Total-variation-diminishing time discretizations, SIAM J. Sci. Stat. Comput. 9 (6) (1988) 1073–1084.
[50] A. Sohankar, C. Norberg, L. Davidson, Low-Reynolds-number flow around a square cylinder at incidence: study of blockage, onset of vortex shedding and outlet boundary condition, Int. J. Numer. Methods Fluids 26 (1998) 39–56.
[51] J.M. Stockie, B.R. Wetton, Analysis of stiffness in the immersed boundary method and implications for time-stepping schemes, J. Comput. Phys. 154 (1998) 41–64.
[52] E.Y. Tau, A second-order projection method for the incompressible Navier–Stokes equations in arbitrary domains, J. Comput. Phys. 115 (1) (1994) 147–152.
[53] A. Thom, Numerical solution for the flow around a cylinder at Reynolds numbers of 40, 200 and 500, Proc. Royal Soc. A 141 (1933) 651–669.
[54] D.J. Tritton, Experiments on the flow past a circular cylinder at low Reynolds number, J. Fluid Mech. 6 (1959) 547.
[55] Y.-H. Tseng, J. Ferziger, A ghost-cell immersed boundary method for flow in complex geometry, J. Comput. Phys. 192 (2003) 593–623.
[56] P.G. Tucker, Z. Pan, A Cartesian cut cell method for incompressible viscous flow, Appl. Math. Model. 24 (2000) 591–606.
[57] H.S. Udaykumar, W. Shyy, M.M. Rao, Elafint: a mixed Eulerian–Lagrangian method for fluid flows with complex and moving boundaries, Int. J. Numer. Method Fluids 22 (1996) 691–705.
[58] H.S. Udaykumar, R. Mittal, W. Shyy, Computation of solid-liquid phase fronts in the sharp interface limit on fixed grids, J. Comput. Phys. 153 (1999) 534–574.
[59] H.S. Udaykumar, R. Mittal, P. Rampunggoon, A. Khanna, A sharp interface Cartesian grid method for simulating flows with complex moving boundaries, J. Comput. Phys. 174 (2001) 345–380.
[60] R.W.C.P. Verstappen, A.E.P. Veldman, Fourth-order DNS of flow past a square cylinder at Re = 22000 – first results, in: J.-P. Chollet, L. Kleiser, P. Voke (Eds.), Direct and Large-Eddy Simulation II, Kluwer Academic Publishers, Dordrecht, 1997, pp. 381–384.
[61] R. Verzicco, J. Mohd-Yusof, P. Orlandi, D. Haworth, LES in complex geometries using boundary body forces, AIAA J. 38 (2000) 427–433.
[62] T. Ye, R. Mittal, H.S. Udaykumar, W. Shyy, An accurate Cartesian grid method for viscous incompressible flows with complex immersed boundaries, J. Comput. Phys. 156 (1999) 20940.